

# Steady-State Modeling and Analysis of a Double-Sided Interior Permanent-Magnet Flat Linear Brushless Motor With Slot-Phase Shift and Alternate Teeth Windings

Young-Shin Kwon and Won-jong Kim

Department of Mechanical Engineering, Texas A&M University, College Station, TX 77843-3123 USA

Analytic modeling techniques of a double-sided interior permanent-magnet flat linear brushless motor (IPM-FLBM) with slot-phase shift and alternate teeth windings are proposed in this paper. Since the buried-type IPM-FLBM with the slot-phase shift and alternate teeth windings is fairly new compared with conventional linear motors, little research has been previously done in modeling and analysis. The analytic models presented in this paper provide the effective and reliable methods for this new type of linear motor. For this purpose, a simplified magnetic equivalent circuit and superposed winding function are investigated. A variable winding function is newly developed in order to evaluate the inductances of the salient motor with the alternate teeth windings. All analytic models are verified with 3-D finite-element analyses (FEAs) step by step. The steady-state thrust force is modeled using a classical closed-form solution for linear brushless ac motors. The static end-effect and cogging forces for the ripple force evaluation are investigated using FEA. The validities for performance parameters are demonstrated experimentally.

*Index Terms*—Alternate teeth windings, linear brushless motor (LBM), slot-phase shift, variable winding function.

## I. INTRODUCTION

NOWADAYS, various types of linear motors are extensively used in high-performance linear motion-control systems as well as high-efficiency energy-harvesting apparatus because of their high force density, fast dynamics, and simple structure compared with the linear platform based on conventional rotary motors. Especially, the linear brushless motor (LBM), which is a type of linear synchronous motor with permanent magnets (PMs) in the mover or stator, is more popular than other types because of various advantages [1], [2]: 1) easy to install the armature coils; 2) easy to assemble the unit modules; 3) easy to adjust the air gap; 4) shorter end-winding length; 5) smaller armature dc resistance; 6) lower space harmonics of the flux distribution; and 7) smaller force ripple. LBMs can be classified into the slotted iron-core and slotless air-core types according to their stators. The LBM can also be characterized as the surface PM (SPM) or IPM types according to its PM configuration. The IPM types can produce the synchronous electromagnetic as well as reluctance forces because of their saliency. In general, the LBM has a trapezoidal or sinusoidal back electromotive force (EMF) profile depending on the air-gap flux-density shape or its winding configuration. In the case of the buried-type IPM-LBM, since its back EMF is close to a sinusoidal rather than trapezoidal waveform [2], its optimal performance can be achieved when it is used in conjunction with vector control. In addition, in the case that the FLBM has the double-sided stators for a mover, a twice larger force can be generated. Therefore, the double-sided IPM-LBM exhibits

Manuscript received December 16, 2015; revised March 30, 2016 and June 8, 2016; accepted July 3, 2016. Date of publication July 11, 2016; date of current version October 17, 2016. Corresponding author: W.-j. Kim (e-mail: wjkim@tamu.edu).

Color versions of one or more of the figures in this paper are available online at <http://ieeexplore.ieee.org>.

Digital Object Identifier 10.1109/TMAG.2016.2589926

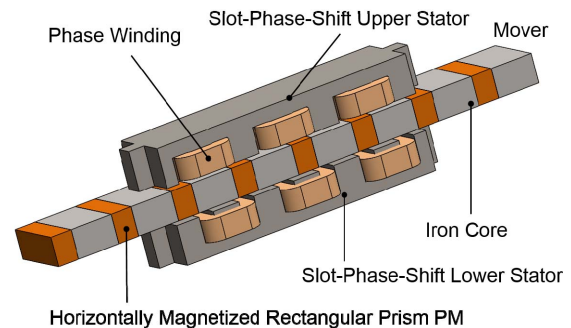


Fig. 1. 3-D rendering for the proposed double-sided 6/4 IPM-FLBM with slot-phase shift and alternate teeth windings.

superior performance in terms of the high force density, low noise, and field weakening compared with other types of linear motors.

However, many studies related to the design, modeling, and performance analysis for linear motors mainly focused on the SPM-FLBMs or tubular linear motors. The magnetic equivalent circuit (MEC) modeling techniques of the single-sided slotted SPM-FLBM were presented in [3]–[5]. The MEC model, design optimization, and experimental verification for the slotted and slotless IPM-tubular linear motors were also presented in [6]–[8]. The performance analysis for the single-sided IPM-FLBM with vertical magnetization and distributed windings was performed in [9]. The modeling and analysis for the double-sided SPM-FLBM and the double-sided flux-switching linear motor were investigated in [10] and [11]. In this sense, this paper presents closed-form modeling techniques for the new double-sided 6/4 (six slots and four poles) IPM-FLBM with slot-phase shift (asymmetric dual three-phase configuration) and alternate teeth windings shown in Fig. 1.

The flowchart in Fig. 2 illustrates the modeling procedure in this paper. First, the mechanical dimension and the electrical

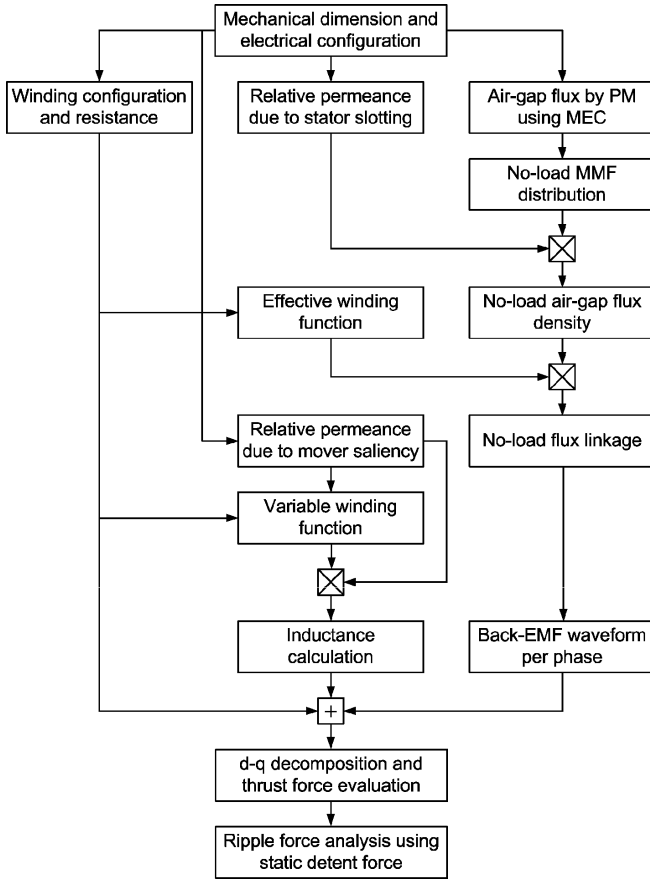


Fig. 2. Analysis flowchart for the double-sided 6/4 IPM-FLBM with the slot-phase shift and alternate teeth windings.

configuration are described. The no-load maximum air-gap flux is estimated using a simplified MEC analysis. The no-load air-gap flux-density function is modeled using the 2-D Fourier series based on the permeance of the stator. The superposed winding functions due to the slot-phase shift between the upper and lower stators are also evaluated. The no-load flux linkages and back EMF voltages are investigated. The inductances are calculated using a new variable winding function, incorporating the saliency of the mover. All analytic models are verified with 3-D finite-element analyses (FEAs) in each modeling step. The steady-state thrust force is derived with a two-phase equivalent-circuit model, and the maximized static thrust force is studied. They are compared with the measured ones. Finally, the static end-effect and cogging forces for the ripple force evaluation are investigated using FEA.

## II. MECHANICAL AND ELECTRICAL DESCRIPTIONS

A cross-sectional schematic in Fig. 3 illustrates the dimension definitions and reference frames of the double-sided 6/4 IPM-FLBM shown in Fig. 1. The step-shaped end frames and slot-phase-shift configuration between the upper and lower stators are employed to reduce the end-effect force and cogging force, respectively [12]. Thus, all teeth centers in the upper stator are shifted by  $\alpha_s$  ahead of the stator centerline, and the lower teeth centers are shifted by  $\alpha_s$  in the opposite direction. The horizontally magnetized PMs are buried in the mover's iron core. The alternate teeth windings with a fractional pitch are used [13]. Each phase consists of two series-connected

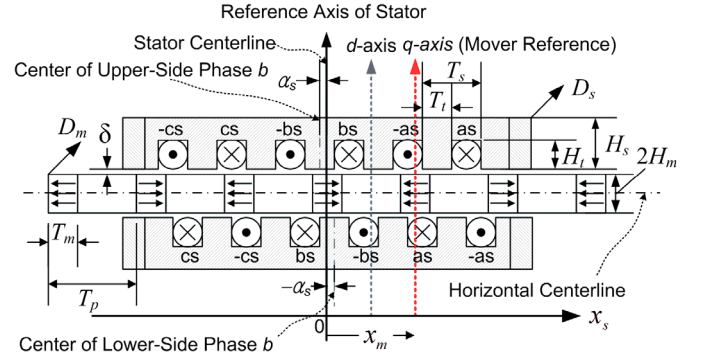


Fig. 3. Cross-sectional dimensions and coordinates of the double-sided 6/4 IPM-FLBM with slot-phase shift and alternate teeth windings.

TABLE I  
MECHANICAL SPECIFICATIONS

Parameters	Symbols	Values (m)
Air gap	$\delta$	0.0010
Stack width of stator	$D_s$	0.0200
Stack width of mover	$D_m$	0.0200
Stator height	$H_s$	0.0110
Stator tooth height	$H_t$	0.0070
One half of PM height	$H_m$	0.0040
PM width	$T_m$	0.0060
Pole pitch	$T_p$	0.0180
Slot pitch	$T_s$	0.0120
Tooth width	$T_t$	0.0076
Slot-phase shift	$\alpha_s$	0.0015

\* SS400 is used for soft-iron core material, and NdFeB 45 for PM.

coils of the upper and lower stators. The stator centerline is chosen as a stator reference axis. The center of the mover iron core with the outgoing magnetic flux is defined as the  $d$ -axis. The  $q$ -axis leads the  $d$ -axis by  $T_p/2$ . The major mechanical parameters of the base model using the electrical solid steel are tabulated in Table I.

## III. MODELING AND ANALYSIS

### A. Magnetic Equivalent Circuit

The classical MEC models for the linear motors presented in [3], [4], and [6] are fast and easy to use, but there is an inaccuracy due to the air-gap permeance model. In contrast, the improved MEC modeling techniques such as hybrid modeling and Schwarz-Christoffel mapping introduced in [5] and [11] can improve the accuracy as well as provide the field distribution in the complex magnetic circuit structure, but they are more difficult to use than the classical method. In this paper, since the maximum no-load flux density is merely needed in the Fourier modeling techniques employed in [3], [10], [13], and [14], the classical MEC is chosen to compute the maximum no-load flux density in air gap. The air-gap permeance model based on Schwarz-Christoffel transform is used in order to overcome the drawbacks of the classical MEC [15].

As shown in Fig. 3, the double-sided IPM-FLBM has a skew-symmetric magnetic circuit with respect to the horizontal centerline of the mover. Hence, the maximum air-gap flux can be calculated from a simplified single-sided MEC model when the  $d$ -axis is aligned with the stator reference axis. Fig. 4(a) and (b) describes the flux path due to the PMs

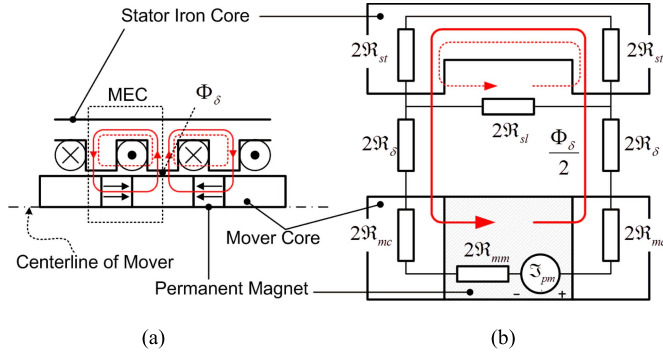


Fig. 4. (a) Flux paths of the single-sided model when the  $d$ -axis is aligned with the stator reference axis under no-load condition. (b) Simplified MEC model with slot leakage reluctance under no-load condition.

and simplified MEC for the flux path in the dashed-lined box, respectively. Since this buried-type IPM structure has a relatively large longitudinal air gap due to the buried PMs, and the magnetomotive force (MMF) of the armature current is significantly smaller than that of the PM as well, an unsaturated model is considered in this paper. The leakage reluctance between teeth is included in the model. The reluctances of the end frames are neglected assuming an infinitely long stator.

From the MEC model, the maximum air-gap flux  $\Phi_\delta$  going into and coming out of the stator teeth can be computed as

$$\Phi_\delta = \frac{\mathfrak{S}_{pm}}{2\mathfrak{R}_\delta + 2\mathfrak{R}_{mc} + \mathfrak{R}_{mm} + \frac{2\mathfrak{R}_{st}\mathfrak{R}_\delta}{2\mathfrak{R}_{st} + \mathfrak{R}_\delta}} \quad (1)$$

where the MMF of the PM is given by

$$\mathfrak{S}_{pm} = \frac{B_r T_m}{\mu_0 \mu_m} \quad (2)$$

where  $B_r$  is the residual flux density ( $= 1.37$  T),  $\mu_0$  is the permeability of free space, and  $\mu_m$  is the relative permeability of the PM ( $= 1.05$ ) on the recoil line on its  $B$ - $H$  curve. Since the mover iron-core width is much larger than the stator's tooth width, the air-gap reluctance with the symmetric fringing flux path should be considered to calculate an accurate air-gap flux. Therefore, the simplified closed-form solution using a Schwarz-Christoffel transformation for the symmetric fringing flux path developed in [15] can be a useful model to calculate the maximum air-gap flux when the  $d$ -axis is aligned with the stator reference axis. The air-gap reluctance is given as

$$\mathfrak{R}_\delta \cong \left\{ \mu_0 D_m \left[ \frac{T_t}{\delta} + \frac{4}{\pi} \left( 1 + \ln \left( \frac{\pi H_t}{4\delta} \right) \right) \right] \right\}^{-1} \quad (3)$$

The reluctance of the PM is calculated as

$$\mathfrak{R}_{mm} = \frac{T_m}{1.55 \mu_0 \mu_m H_m D_m} \quad (4)$$

where the factor 1.55 is used to describe the effective contact face area reduced due to the PM with the H-shaped cross section and all round edges with a radius of about 0.5 mm. The slot leakage, mover iron core [16], and stator tooth reluctances are obtained as

$$\mathfrak{R}_{sl} = \frac{T_s - T_t}{2\mu_0 H_t D_s} \quad (5)$$

$$\mathfrak{R}_{mc} = \frac{\pi}{8\mu_0 \mu_c D_m} \quad (6)$$

$$\mathfrak{R}_{st} = \frac{2H_t + H_b}{2\mu_0 \mu_c T_t D_s} \quad (7)$$

where  $\mu_c$  is the relative permeability of the iron core and the back-iron thickness  $H_b$  is  $H_s - H_t$ . When the maximum permeability value is given as 1550, the flux in the air gap is estimated as 0.1417 mWb from (1).

### B. No-Load Flux Density and Stator's Relative Permeance

The air-gap MMF is produced by the armature currents and PMs. Especially, the air-gap MMF due to the PMs is the fundamental source of the thrust force in PM linear motors. The maximum air-gap MMF due to the PMs is given by

$$\mathfrak{S}_m = \mathfrak{R}_\delta \Phi_\delta. \quad (8)$$

Assuming the stator to have smooth surfaces, the no-load air-gap MMF distribution function according to the mover positions with respect to the stator reference axis can be represented as a Fourier series

$$\mathfrak{S}_\delta(x_s, x_m) = \mathfrak{S}_m \sum_{n=1,3,5,\dots}^{\infty} F_n \sin \left( \frac{\pi n (x_m - x_s)}{T_p} \right) \quad [A] \quad (9)$$

where the  $n$ th spatial harmonic component  $F_n$  is given by

$$F_n = (-1)^{\frac{n-1}{2}} \frac{8}{n\pi} \cdot \frac{\cos(n\pi(T_p - T_m)/2T_p)}{n\pi(T_p - T_m)/2T_p}. \quad (10)$$

The no-load air-gap flux-density function of the slotted linear motor can also be given by the product of the no-load air-gap MMF and permeance of the stator as in [10] and [14]

$$B_\delta(x_s, x_m, \alpha_s) = \frac{\mu_0}{\delta} P_s(x_s, \alpha_s) \mathfrak{S}_\delta(x_s, x_m) \quad [T] \quad (11)$$

where the relative permeance function of the stator  $P_s(x_s, \alpha_s)$  has a value between zero and one, and  $\alpha_s$  is the slot-phase shift. The actual air-gap flux density is distributed nonlinearly in the slot opening. This slotting affects the distribution of the air-gap flux density as well as decreases the total flux per pole. Several models have been introduced previously to consider such slotting effects [14], [17]. Likewise, the stator model with the infinitely deep rectilinear slots is used to derive the relative permeance function of the stator as

$$P_s(x_s, \alpha_s) = P_0 + (1 - P_0) \left| \sum_{n=1,3,5,\dots}^{\infty} P_n \cos \left( \frac{n\pi}{T_s} (x_s + \alpha_s) \right) \right| \quad (12)$$

where  $P_0$  is calculated as

$$P_0 = K_{cs} \frac{2u_s}{1 + u_s^2} \quad (13)$$

where the Carter coefficient  $K_{cs}$  and  $u_s$  are calculated as

$$K_{cs} = \frac{T_s}{T_s - T_{seo}} = \frac{T_s}{T_s - k_s T_{so}}$$

and

$$u_s = \frac{T_{so}}{2\delta} + \sqrt{1 + \left( \frac{T_{so}}{2\delta} \right)^2} \quad (14)$$

where the slot opening  $T_{so}$  is  $T_s - T_t$ , and  $k_s$  is determined by

$$k_s \approx \frac{T_{so}}{5\delta + T_{so}} \quad (15)$$

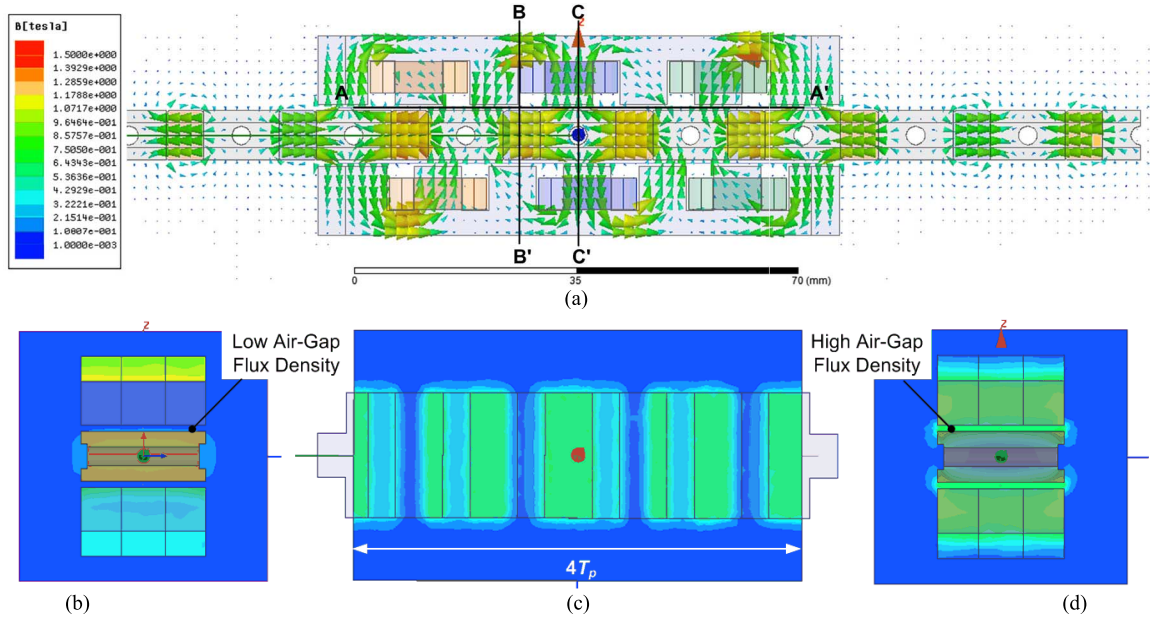


Fig. 5. (a) FE flux-density vector paths in the midcross-section plane. (b) Flux-density distribution in the cut-through section B-B'. (c) Flux-density distribution in the midplane A-A' of the air gap between the upper stator and the mover. (d) Flux-density distribution in the cut-through section C-C' when the  $d$ -axis is aligned with the stator reference axis under the no-load condition.

and the  $n$ th harmonic component  $P_n$  is computed as

$$P_n = (-1)^{\frac{n-1}{2}} \frac{4}{\pi} \cdot \frac{\sin(n\pi(1-k_s)T_{so}/4T_s)}{n\pi(1-k_s)T_{so}/4T_s} \times \cos\left(\frac{n\pi(1+k_s)T_{so}}{4T_s}\right). \quad (16)$$

The result in Fig. 5(a) shows the flux-density vector paths and magnitude in the midcross-section plane of the 3-D FEA when the  $d$ -axis is aligned with the stator reference axis under the no-load condition. The flux-density contour plots of the midplane A-A' in Fig. 5(b) and the cut-through sections B-B' and C-C' in Fig. 5(c) and (d) show that the flux-density distribution for the flux vector in the midcross-section plane can be used as a typical distribution in this short-stack-width linear motor because it is uniformly distributed in the entire stack width. Fig. 6(top) and (bottom) illustrates the air-gap flux-density distributions of the upper and lower sides including the slot-phase shift and slotting effect in the upper and lower air gaps. The analytic models with a maximum air-gap flux density of 0.642 T are in good agreement with the FEA results of 0.639 T. This implies that the air-gap flux and relative permeance functions are modeled accurately.

### C. DC Resistance of Armature Winding

The armature dc resistance is one of the most important electrical parameters in electric machines from the efficiency point of view. Assuming that the skin effect by the alternating current and the flux in the winding are negligible, the dc resistance calculation of the uniformly concentrated rectangular winding is straightforward. Fig. 7(a) and (b) shows the dimensions and photograph of the uniformly concentrated rectangular armature winding used in this paper.

The dc resistance of a winding is dependent on the operation temperature of the electric machine. The variation of armature

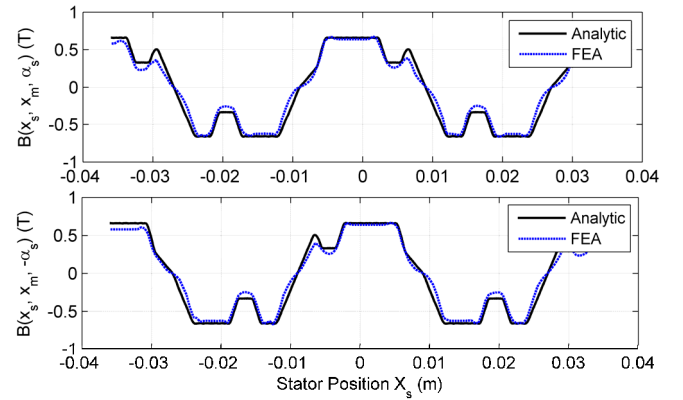


Fig. 6. Predicted air-gap flux density distributions for the upper-side (top) and lower-side (bottom) air gaps when the  $d$ -axis is aligned with the stator reference axis under the no-load condition.

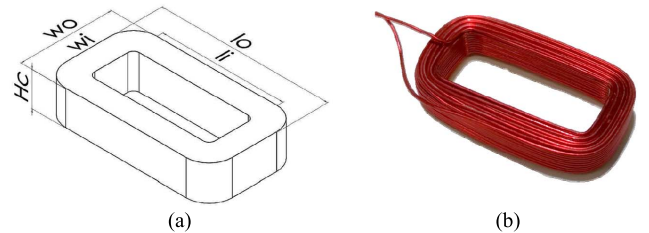


Fig. 7. Uniformly concentrated rectangular winding. (a) Dimension definitions of the armature winding. (b) Photograph of the armature winding.

resistance in the temperature range from 0 °C to 150 °C is expressed by

$$R_a = R_{20}(1 + \alpha_{20}(T - 20^\circ)) \quad (17)$$

where  $R_{20}$  and  $\alpha_{20}$  are the resistance and the temperature coefficient at 20 °C, respectively,  $T$  is the given temperature, and  $\alpha_{20}$  is 0.00393 1/°C for the copper wire. According to

Ohm's law, the resistance  $R_{20}$  at 20 °C is given by

$$R_{20} = \frac{\rho_{cu} l_{cu}}{S_{cu}} = \frac{4\rho_{cu} l_{ac} N}{\pi D_c^2} \quad (18)$$

where  $\rho_{cu}$  is the resistivity of copper ( $1.7 \times 10^{-8} \Omega \cdot \text{m}$ ),  $l_{cu}$  is the total length of a winding, and  $S_{cu}$  and  $D_c$  are the cross-sectional area of the conductor and the diameter of the copper wire, respectively. The average length  $l_{ac}$  per turn can be estimated as  $2T_s + l_o + l_i$ , where  $l_o$  and  $l_i$  are the outer and inner lengths of a coil, respectively. The number of turns  $N$  per winding can be calculated as

$$N = \frac{k_f A_{cu}}{D_{ci}^2} = \frac{k_f H_c T_{so}}{D_{ci}^2} \quad (19)$$

where  $D_{ci}$  is the diameter of copper wire with the insulation layer,  $A_{cu}$  is the cross-sectional area of the slot,  $k_f$  is the fill factor of the slot, and  $H_c$  is the coil height. From (17) and (18), the dc resistance per winding can be written as

$$R_a = [4\rho_{cu} l_{ac} N (1 + \alpha_{20}(T - 20^\circ))] / \pi D_c^2. \quad (20)$$

where  $H_c$ ,  $l_o$ ,  $l_i$ , the outer width  $w_o$ , and the inner width  $w_i$  of a winding were chosen as 0.005, 0.028, 0.021, 0.016, and 0.0078 m, respectively. The wire of the diameter  $D_{ci}$  of 0.00045 m (bondable cooper wire of 26 AWG) was used. As a result, the number of turns of 85 was achieved. The dc resistance per winding was calculated as 0.825 and 1.25  $\Omega$  at 20 °C and 150 °C, respectively. The actual resistance per winding was measured as 0.836  $\Omega$ . Thus, the total dc resistance per phase of the double-sided model became 1.672  $\Omega$ .

#### D. No-Load Flux Linkage and Back EMF Voltage

The total flux linkage in the IPM-FLBM is expressed as

$$\lambda_{phase} = \lambda_a + \lambda_{pm} \quad (21)$$

where  $\lambda_a$  is the armature flux linkage due to the phase currents and  $\lambda_{pm}$  is the no-load flux linkage due to the mover PMs. The no-load flux linkage of a winding is maximized when the  $d$ -axis is aligned with the centerline of the winding tooth of each winding. The no-load flux linkage per winding with the slot-phase shift can be calculated as follows.

$$\lambda_{pm\_coil}(x_m, \alpha_s, \beta) = D_s \int_{-2T_p}^{2T_p} N(x_s, \alpha_s, \beta) B_\delta(x_s, x_m, \alpha_s) dx_s \quad (22)$$

where  $N(x_s, \alpha_s, \beta)$  is the generalized winding function [18], and  $\beta$  is  $-2T_s$ , 0, and  $2T_s$  for phases  $a$ ,  $b$ , and  $c$ , respectively. The slot-phase-shift term is  $\alpha_s$  and  $-\alpha_s$  for the upper and lower stators, respectively. Assuming the stator has a smooth surface, the generalized winding function is given as

$$N(x_s, \alpha_s, \beta) = n(x_s, \alpha_s, \beta) - \langle n(x_s, \alpha_s, \beta) \rangle \quad (23)$$

where the first term of the right-hand side is the turns function and the second term is the average turns function. Therefore, if each winding is uniformly concentrated as illustrated in Fig. 7 and has the period of  $2T_s$  by the alternate teeth winding

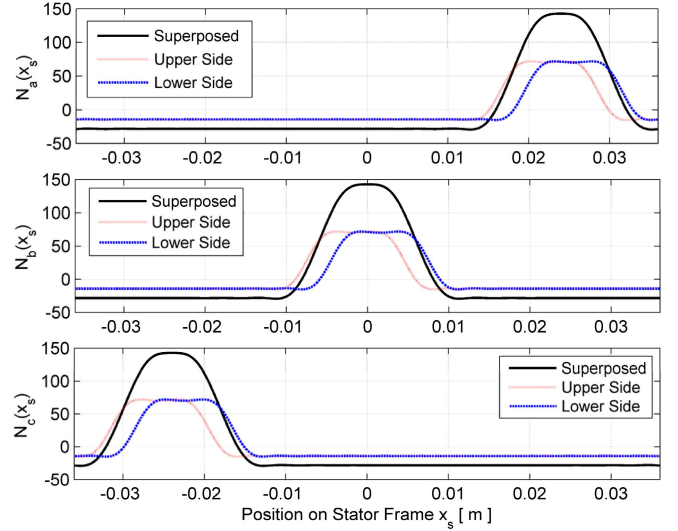


Fig. 8. Superposed winding functions of phases  $a$ ,  $b$ , and  $c$  when a coil has the number of turns of 85.

arrangement, the winding function with the slot-phase shift can be written in the form of a Fourier series as follows.

$$N(x_s, \alpha_s, \beta) = 2N \sum_{n=1}^{\infty} N_n \frac{\sin(n\pi/4)}{n\pi} \cos\left(\frac{n\pi(x_s + \beta + \alpha_s)}{2T_p}\right) \quad (24)$$

where the  $n$ th spatial harmonic winding factor  $N_n$  for the uniformly concentrated winding is given by

$$N_n = \frac{4T_p}{n\pi T_{so}} \sin\left(\frac{n\pi T_s}{4T_p}\right) \sin\left(\frac{n\pi T_{so}}{4T_p}\right). \quad (25)$$

From (24), six winding functions are developed, and a pair of winding functions for the same phase have the offset of  $T_s/6$  between each other. However, since the windings of the upper and lower stators for the same phase are connected in series, the two winding functions of the upper and lower sides are spatially superposed. Consequently, the new three superposed winding functions can be derived as

$$\begin{aligned} N_{phase}(x_s, \beta) &= N(x_s, \alpha_s, \beta) + N(x_s, -\alpha_s, \beta) \\ &= 4N \sum_{n=1}^{\infty} N_n \frac{\sin(n\pi/4)}{n\pi} \cos\left(\frac{n\pi \alpha_s}{2T_p}\right) \\ &\quad \times \cos\left(\frac{n\pi(x_s + \beta)}{2T_p}\right). \end{aligned} \quad (26)$$

Fig. 8 shows the six slot-phase-shift winding functions and the new three superposed winding functions for each phase.

Eventually, the no-load flux linkages for each phase can be obtained using the superposed winding functions (26) and the air-gap flux-density function (11) as follows.

$$\lambda_{pm\_phase}(x_m, \beta) = D_s \int_{-2T_p}^{2T_p} N_{phase}(x_s, \beta) B_\delta(x_s, x_m, 0) dx_s \quad (27)$$

Fig. 9 illustrates that the no-load flux linkages of (27) have the sinusoidal waveforms. As expected, the maximum

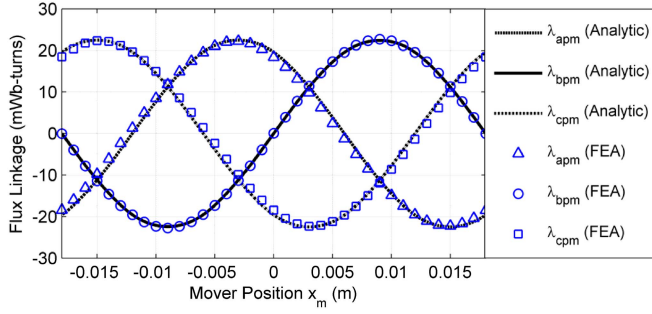


Fig. 9. Analytic and FEA results of the no-load flux linkages for each phase according to the mover positions.

no-load flux linkage for each phase occurs when the  $d$ -axis is aligned with the superposed winding centerline rather than the individual winding tooth centerline. This good agreement between the FEA and the analytic solution indicates that the superposed winding function is valid in the slot-phase-shift structure. The maximum flux linkages for phase  $b$  in the analytic solution and the FEA are calculated as around 21.8-mWb turns and simulated as 22.1-mWb turns, respectively.

The phase-to-neutral back EMF can be derived through differentiating the flux linkage in (27) for the mover displacement  $x_m$  with respect to time as follows.

$$e_{phase}(x_m, \beta) = \frac{d\lambda_{pm}}{dt} = D_s \int_{-2T_p}^{2T_p} N_{phase}(x_s, \beta) \times \frac{dB_{\delta}(x_s, x_m, 0)}{dt} dx_s \quad (28)$$

Fig. 10 shows that the phase-to-neutral back EMFs of the analytic model are in good agreement with the FEA results for each phase. The eddy-current loss is not considered in this simulation. The phase-to-neutral back-EMF constants in the FEA and the analytic solution are evaluated as 3.93 V-s/m and are computed as 3.75–3.95 V-s/m, respectively.

### E. Inductance Calculations

The self-inductance consists of the magnetizing, harmonic-leakage, slot-leakage, end-winding-leakage, and tooth-top-leakage (zigzag-leakage) inductances [17], [18]. The end-winding- and tooth-top-leakage inductances in a common design practice are often ignored because their values are much smaller than other components. Thus, it is assumed that the tooth-top-leakage inductance of the open slot is negligible in this paper. However, since the end-winding-leakage inductance cannot be ignored in the nonoverlapping winding machine with a short stack width close to the pole pitch [19], the self-inductance of a phase configured with two series-connected nonoverlapping concentrated windings of the upper and lower stators can be expressed as

$$L_s(x_m) = (Q/3)L_u + (Q/6)L_{ew} + L_m(x_m) \quad (29)$$

where  $L_u$  is the slot leakage inductance per slot,  $Q$  is the total slot number of the upper and lower stators,  $L_{ew}$  is the end-winding-leakage inductance per winding, and  $L_m$  is the total magnetizing inductance per phase. In the case of the iron-core SPM configured with the distributed winding, the

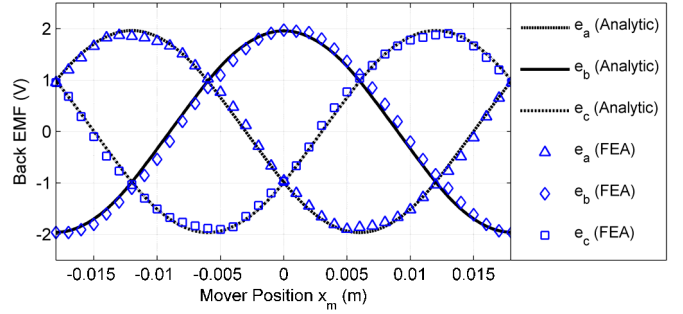


Fig. 10. Analytic and FEA results of the phase-to-neutral back EMFs for each phase when the mover has a linear speed of 0.5 m/s.

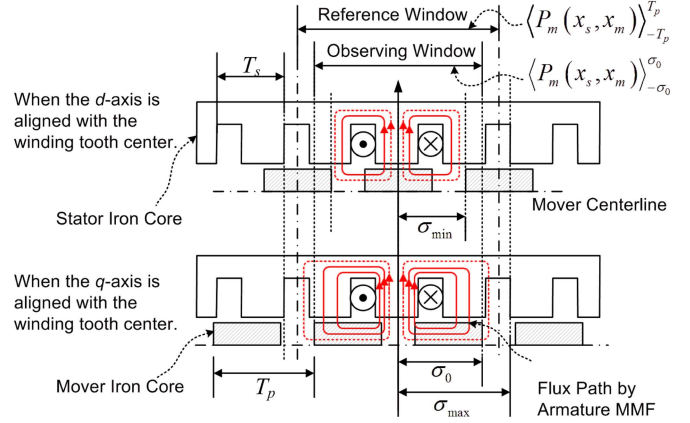


Fig. 11. Variable winding function model in the IPM-FLBM: flux paths when the  $d$ -axis is aligned with the winding tooth center (top) and when the  $q$ -axis is aligned with the winding tooth center (bottom).

magnetizing inductance can be calculated using the generalized winding function given in (23) and constant air gap. This is because the generalized winding function is defined under the assumption that the sum of incoming and outgoing fluxes in the entire air gap between the stator and mover is zero as follows.

$$\int_0^{2\pi} N(\theta_s) d\theta_s = 0 \quad (30)$$

where  $\theta_s$  is the angle of the stator. However, as shown in Fig. 11(top) and (bottom), the fluxes induced by the armature MMF in the buried-type IPM configuration are not distributed in the entire air gap because of the alternate teeth windings and the large air gap between the mover iron cores. Thus, the generalized winding function is unavailable to calculate the inductance of this configuration. Furthermore, the generalized winding function cannot evaluate the variation of the maximum magnitude of MMF in the air gap according to the mover positions. For example, when the  $d$ -axis is aligned with the winding tooth center as shown in Fig. 11(top), the air-gap flux density is significantly decreased due to the large air gap between the stator teeth and both sides of the iron core, and its magnitude is much less when the  $q$ -axis is aligned with the same tooth center as shown in Fig. 11(bottom). However, since the inductance calculation using (24) can evaluate only the cross-sectional area corresponding to the mover permeance profile, the inductance of the  $d$ -axis is calculated to be a much larger value than that of the  $q$ -axis.

Therefore, a new variable winding function based on the modified winding function [20] is developed in this paper. The variable winding function has the flux distribution range from  $2\sigma_{min}$  to  $2\sigma_{max}$ . They are determined by the variation of the average permeance of the observing window according to the mover position versus the average permeance of the reference window. The distribution range variable  $\sigma$  with respect to the winding tooth center can be calculated as

$$\sigma = \sigma_0 + \frac{k}{2} [\langle P_m(x_s, x_m) \rangle_{-\sigma_0}^{\sigma_0} - \langle P_m(x_s, x_m) \rangle_{-T_p}^{T_p}] \quad (31)$$

where  $\langle P_m(x_s, x_m) \rangle$  is the average relative permeance function of the mover in a given range. The relative permeance function of the mover is given as

$$P_m(x_s, x_m) = P_0 + (1 - P_0) \times \left| \sum_{n=1,3,5,\dots}^{\infty} P_n \cos\left(\frac{n\pi}{T_p}(x_s - x_m) - \frac{n\pi}{2}\right) \right| \quad (32)$$

where all coefficients in (32) can be calculated using (13)–(16) after replacing  $T_s$  and  $T_{s0}$  with  $T_p$  and  $T_m$ , respectively. The observing range  $2\sigma_0$  is given as  $2T_p - T_m$  from Fig. 11. The coefficient  $k$  is chosen as a number that makes the minimum value of the calculation result of (31) be equal to  $\sigma_{min}$  ( $= 2T_s$ ), as shown in Fig. 11. The new winding function of phase  $b$  in the upper side using the variable range is given by

$$VM_x(x_s, x_m, \alpha_s) = n_x(x_s, \alpha_s) - \frac{\int_{-\sigma}^{\sigma} n_x(x_s, \alpha_s) P_m(x_s, x_m) dx_s}{2\sigma \langle P_m(x_s, x_m) \rangle_{-\sigma}^{\sigma}}. \quad (33)$$

The variable winding function in the lower side can be achieved replacing  $\alpha_s$  with  $-\alpha_s$ . Fig. 12 illustrates that both the magnitude and the distribution range are minimized when the  $d$ -axis is aligned with the winding tooth center, and they are maximized when the  $q$ -axis is aligned with the winding tooth center.

Therefore, the magnetizing inductance of the double-sided IPM-FLBM using (33) can be represented as

$$L_{xm}(x_m) = \frac{\mu_0 D_s}{\delta} \int_{-2T_p}^{2T_p} (VM_x^2(x_s, x_m, \alpha_s) + VM_x^2(x_s, x_m, -\alpha_s)) \times P_m(x_s, x_m) dx_s \quad (34)$$

where the subscript  $x$  represents each phase. Similarly, the mutual inductance is also given as

$$L_{xy}(x_m) = \frac{\mu_0 D_s}{\delta} \int_{-2T_p}^{2T_p} (VM_x(x_s, x_m, \alpha_s) VM_y(x_s, x_m, \alpha_s) + VM_x(x_s, x_m, -\alpha_s) VM_y(x_s, x_m, -\alpha_s)) P_m(x_s, x_m) dx_s. \quad (35)$$

The slot-leakage inductance per slot is calculated as 0.151 mH using a classical equation as [17]

$$L_u = \frac{\mu_0 D_s N^2}{T_{s0}} \left( H_t - \frac{2}{3} H_c \right). \quad (36)$$

The analytic model for the end-winding-leakage inductance in the nonoverlapping winding PM machine is developed

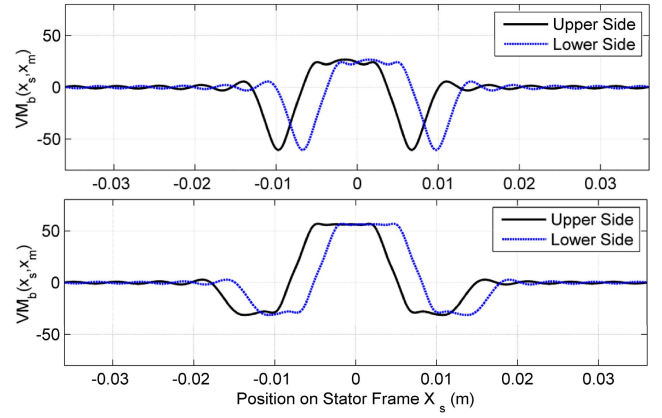


Fig. 12. Variable winding function of phase  $b$  in the upper and lower sides when the  $d$ -axis is aligned with the stator reference axis (top) and when the  $q$ -axis is aligned with the stator reference axis (bottom).

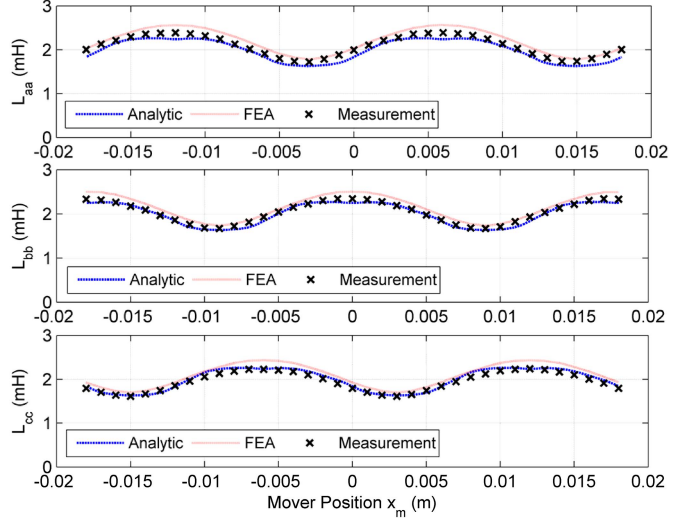


Fig. 13. Self-inductance distributions of each phase according to the mover positions.

in [19]. This equation takes the end-winding geometry and laminated stack effect into account. If adopting this equation into the double-sided IPM linear motor, since the average coil radius can be assumed to be  $3T_s/\pi$ , the end-winding-leakage inductance per winding can be expressed as

$$L_{ew} = 1.257 \left( \frac{6T_s l_e}{\pi(w_o - w_i)} \right) K N^2 \quad (37)$$

where the average end length  $l_e$  is  $w_o + (l_i - D_s)/2$  and the constant  $K$  is given as

$$K = k_1 - k_2 \quad (38)$$

where  $k_1$  and  $k_2$  are written as a function of the dimensional variables  $a$ ,  $b$ , and  $c$  in [19]. These variables can be given as  $3T_s/\pi$ ,  $w_o - w_i$ , and  $H_c$ , respectively, in the double-sided IPM-FLBM. The end-winding-leakage inductance per winding is computed as 0.140 mH.

The self-inductance distributions in Fig. 13 illustrate that each inductance has its maximum value when the  $q$ -axis is aligned with the corresponding superposed axis. Although the

TABLE II  
AVERAGE VALUES OF INDUCTANCES

	$L_{aa}$	$L_{bb}$	$L_{cc}$	$L_{ab}, L_{ba}$	$L_{bc}, L_{cb}$	$L_{ac}, L_{ca}$
Measured (mH)	2.092	2.042	1.952	-0.065	-0.067	-0.010
FE analysis (mH)	2.200	2.200	2.200	-0.078	-0.078	-0.007
Calculated (mH)	2.151	2.150	2.151	-0.054	-0.054	-0.011

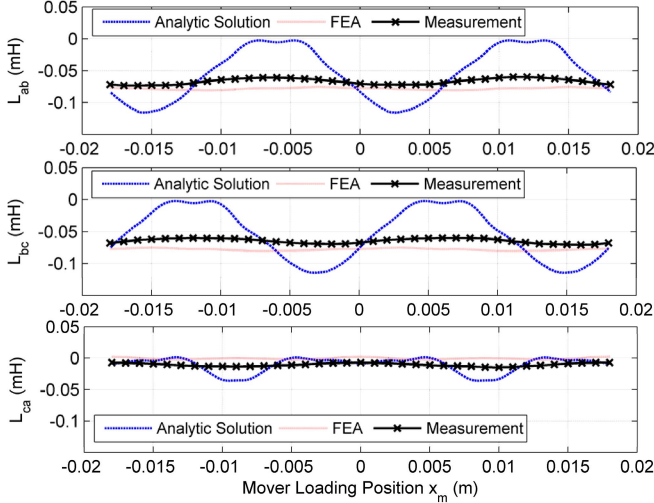


Fig. 14. Mutual inductance distributions of each phase according to the mover positions.

FEA results and analytic solutions have slightly larger values than those of the measured self-inductances, they are in good agreement with each other in the perspective of a function of mover position. The average self-inductance comparison in Table II shows that the measured self-inductances have around 7% smaller values than FEA results and analytic solutions.

As shown in Fig. 11, since the passive teeth in the alternate-teeth-winding configuration play the role of the alternate flux path, the mutual flux linkages between two adjacent phase windings have very small values [13]. Especially, the mutual inductance  $L_{ac}$  between phases  $a$  and  $c$  is much closer to zero because the linear motor stator has the open circuit in its end frame. The mutual inductances in Fig. 14 obtained from the analytic solution, FEA, and measurement illustrate such an expected behavior. Although the varying amplitude of the analytic solution is much larger than those of the measured inductances because of the resolution limitation of the winding function model based on the Fourier series, its trend according to the mover positions is in good agreement with the measurement one, and its average value is within the error of 20%. The FEA result shows the much more ideal case than others. This result also implies that the mutual inductances' roles in electromagnetic circuit are negligible compared with the self-inductances. The average mutual inductance comparison in Table II implies that our analytic inductance models are well established, as well as the mutual inductance has around 3% of the self-inductance value in the alternate-teeth-winding configuration. This value is even smaller than those of the conventional all teeth winding or sinusoidal winding structure.

#### IV. THRUST-FORCE CALCULATION

In this section, the steady-state thrust-force calculation is presented using the  $d$ - $q$  model of the three-phase IPM-FLBM.

On the basis of the analyses presented in Section III, the following assumptions are made: 1) the no-load flux linkage is sinusoidal, and the space harmonics in the air gap are neglected; 2) the armature linkage flux is also sinusoidal, and the space harmonics in the air gap are neglected; 3) the balanced three-phase currents and voltages are considered; and 4) the eddy-current and hysteretic effects are neglected.

#### A. Terminal-Voltage Equations

The matrix form of the terminal-voltage equations in terms of the phase currents and no-load flux linkages is given by

$$\begin{bmatrix} v_a \\ v_b \\ v_c \end{bmatrix} = \begin{bmatrix} R_a & 0 & 0 \\ 0 & R_a & 0 \\ 0 & 0 & R_a \end{bmatrix} \begin{bmatrix} i_{as} \\ i_{bs} \\ i_{cs} \end{bmatrix} + \frac{d}{dt} \left( \begin{bmatrix} L_{aa} & L_{ab} & L_{ac} \\ L_{ba} & L_{bb} & L_{bc} \\ L_{ca} & L_{cb} & L_{cc} \end{bmatrix} \begin{bmatrix} i_{as} \\ i_{bs} \\ i_{cs} \end{bmatrix} + \begin{bmatrix} \lambda_{ma} \\ \lambda_{mb} \\ \lambda_{mc} \end{bmatrix} \right) \quad (39)$$

where the balanced three-phase armature currents  $i_{as}$ ,  $i_{bs}$ , and  $i_{cs}$  are given by

$$\mathbf{i}_{abc} = I_m \begin{bmatrix} \cos(\omega_e t + 2\pi/3) \\ \cos(\omega_e t) \\ \cos(\omega_e t - 2\pi/3) \end{bmatrix} \quad (40)$$

where  $I_m$  is the magnitude of the applied current, and  $\omega_e$  is the electric frequency. The no-load linkage terms can be given from the results in Fig. 9 and the assumption in this section as

$$\lambda_m = \begin{bmatrix} \lambda_{ma} \\ \lambda_{mb} \\ \lambda_{mc} \end{bmatrix} = \lambda_m \begin{bmatrix} \sin(\theta + 2\pi/3) \\ \sin(\theta) \\ \sin(\theta - 2\pi/3) \end{bmatrix} \quad (41)$$

where  $\theta = \pi x_m / T_p$ . According to [21], the generalized inductance of the salient PM synchronous motor can be modeled with the function of the mover positions as follows.

$$\begin{aligned} L_{aa}(x_m) &= 4L_u + 2L_{ew} + L_{ma}(x_m) \\ &= L_{ls} + L_{os} + L_{2s} \cos(2(\theta + 2\pi/3)) \\ L_{bb}(x_m) &= 4L_u + 2L_{ew} + L_{mb}(x_m) \\ &= L_{ls} + L_{os} + L_{2s} \cos(2\theta) \\ L_{cc}(x_m) &= 4L_u + 2L_{ew} + L_{mc}(x_m) \\ &= L_{ls} + L_{os} + L_{2s} \cos(2(\theta - 2\pi/3)) \end{aligned} \quad (42)$$

where  $L_{ma}$ ,  $L_{mb}$ , and  $L_{mc}$  are the magnetizing inductances of each phase,  $L_{ls}$  is the sum of the leakage inductance,  $L_{os}$  is the constant value of the magnetizing inductance, and  $L_{2s}$  is the amplitude of the second-harmonic term of the magnetizing inductance. From the inductance-distribution plots in Fig. 13 and Table II,  $L_{ls}$ ,  $L_{os}$ , and  $L_{2s}$  in (42) can be evaluated as 0.886, 1.12, and 0.34 mH, respectively. From Fig. 14 and Table II, the mutual inductances are assumed to be zeros in the inductance matrix of (39) as follows.

$$\begin{aligned} L_{ab}(x_m) &= L_{ba}(x_m) = L_{bc}(x_m) = L_{cb}(x_m) \\ &= L_{ca}(x_m) = L_{ca}(x_m) \approx 0. \end{aligned} \quad (43)$$

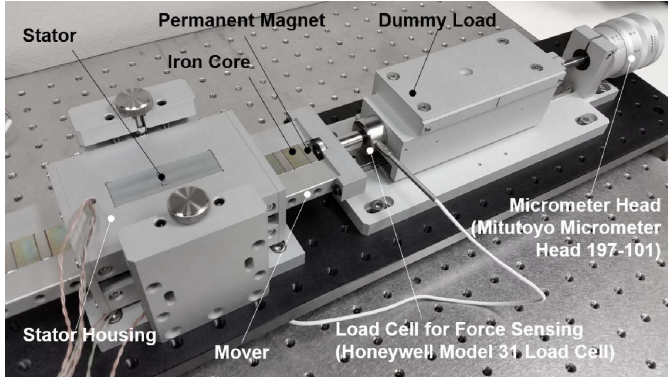


Fig. 15. Photograph of the experimental setup to measure the inductances and steady-state thrust forces.

### B. Steady-State Thrust-Force Calculation

In the rotary machine, the terminal voltage equations of the two-phase circuit through the  $d$ - $q$  decomposition of (39) are given as

$$\begin{aligned} V_{qs} &= (R_s + L_q p)I_{qs} + \omega_m L_d I_{ds} + \omega_m \lambda_{dm} \\ V_{ds} &= (R_s + L_d p)I_{ds} - \omega_m L_q I_{qs} \end{aligned} \quad (44)$$

where  $p$  is  $d/dt$ ,  $I_q$  and  $I_d$  are the  $q$ -axis and  $d$ -axis currents,  $\omega_m$  is the mechanical angular speed, and  $\lambda_{dm}$  is the  $d$ -axis flux linkage. According to [21], the generalized forms for the  $q$ - and  $d$ -axis inductances  $L_q$  and  $L_d$  in the salient pole machine are given as

$$L_q = L_{ls} + L_{os} + L_{2s}$$

and

$$L_d = L_{ls} + L_{os} - L_{2s}. \quad (45)$$

Thus, the  $q$ - and  $d$ -axis inductances are calculated as 2.34 and 1.66 mH, respectively. Since the linear speed  $V_m$  of the linear motor is equal to the synchronous speed of the traveling magnetic field, the linear and rotating speeds have the following relationship:

$$V_m = \omega_m T_p / \pi. \quad (46)$$

From (44)–(46), the terminal voltage equations according to the mover speed can be written as

$$\begin{aligned} V_{qs} &= (R_s + L_q p)I_{qs} + \frac{\pi}{T_p} (L_d I_{ds} + \lambda_{dm}) V_m \\ V_{ds} &= (R_s + L_d p)I_{ds} - \frac{\pi}{T_p} L_q I_{qs} V_m. \end{aligned} \quad (47)$$

The mechanical power can be obtained by subtracting the ohmic loss and the rate of the change of the stored energy in the magnetic circuit from the instantaneous power computed with (47) [20]. The developed thrust force can be expressed in terms of the  $d$ - and  $q$ -axis current as follows.

$$F_x = \frac{3\pi}{2T_p} (\lambda_{dm} I_{qs} + (L_d - L_q) I_{ds} I_{qs}) \quad (48)$$

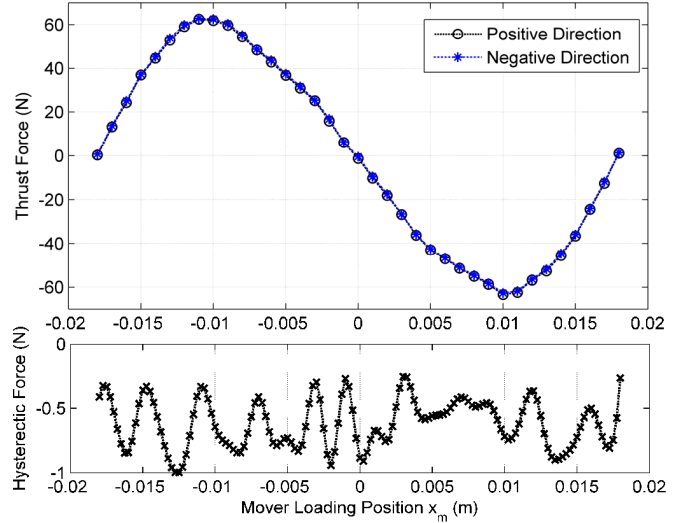


Fig. 16. Measured static forces according to the moving direction when  $I_a = I_c = 8.66$  A and  $I_b = 0$  A (top) and the static force differences between the positive and negative entry directions at the same positions (bottom).

### V. STEADY-STATE FORCE VALIDATION

Fig. 15 shows the experimental setup that measures the inductances and steady-state thrust forces of the double-sided 6/4 IPM-FLBM modeled in this paper. A 300-W dc power supply was used. A precision bidirectional load cell with a 0.1% nonlinearity and a micrometer head with an accuracy of  $\pm 0.0005$  mm were employed in order to measure the steady-state thrust forces according to the mover positions. The inductances were measured using a 120-Hz sinusoidal current source of 1.0 A.

In theory, the resultant force superposed by the upper and lower stators with slot-phase shift is developed with respect to the new stator reference axis. It is not affected by the direction of motion of the mover. However, the results in Fig. 16 show that there are small differences in the static forces according to the mover's direction and position. This implies that the actual IPM-FLBM has the average hysteretic force of  $-0.6$  N depending on the entry direction of the mover although its value is much less than the maximum force. This hysteretic force seems to be caused by the imperfections in the mechanical structure and PM.

The thrust force of (48) is composed of two distinct mechanisms. The first term corresponds to the magnetizing force occurring between  $I_{qs}$  and the PM, whereas the second term is the reluctance force generated due to the differences between the  $d$ - and  $q$ -axis inductances. Assuming that the supply voltage and current are limited and that the supplied current vector leads the  $q$ -axis current by the phase angle  $\gamma$ , in steady state, (48) can be rewritten using the magnitude of the current vector  $I_s$  as

$$F_x = \frac{3\pi}{2T_p} \left( \lambda_m I_s \cos \gamma + \frac{1}{2} (L_q - L_d) I_s^2 \sin 2\gamma \right) \quad (49)$$

where  $I_s$  is given as

$$I_s = \sqrt{I_q^2 + I_d^2}. \quad (50)$$

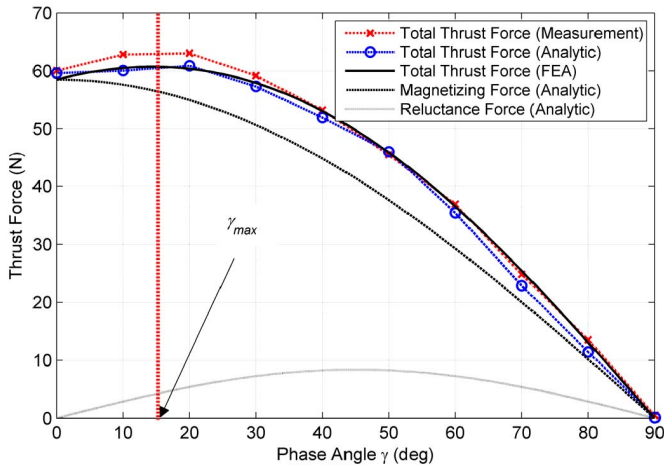


Fig. 17. Thrust force components according to the current phase angle  $\gamma$  when the magnitude of the current vector  $I_s$  of 10 A is applied.

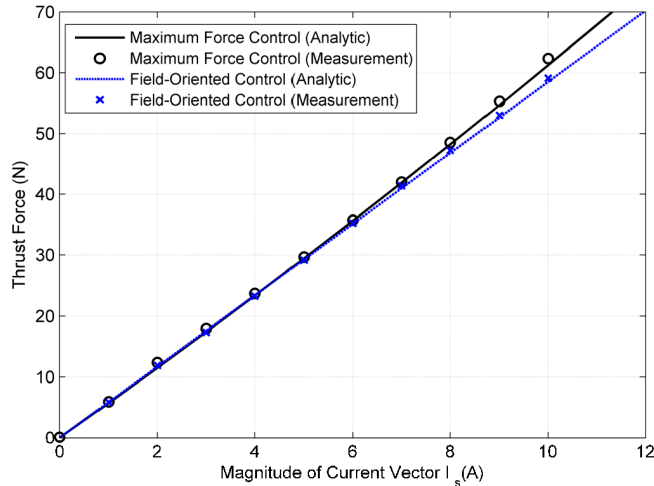


Fig. 18. Force-to-current ratios in the MFC and FOC schemes.

Thus, the maximized thrust force can be obtained through field weakening due to the  $d$ -axis armature reaction. Fig. 17 shows that the maximum thrust force is produced when the phase angle  $[\text{= } \tan^{-1}(I_d/I_q)]$  is around  $15^\circ$  although the reluctance force at a current vector of 10 A is not significantly large due to the small difference between the  $q$ - and  $d$ -axis inductances. The measured total thrust forces are achieved within maximum 2% error when compared with the total thrust forces in the calculation and FEA. The predicted total thrust force using a closed-form analysis matches quite well with the measurement and FEA.

Fig. 18 shows that the maximum force control (MFC) scheme using the reluctance force can produce more force than that of the field-oriented-control (FOC) scheme for the same input power. This implies that if the residual flux density of the PM is not deteriorated by the  $d$ -axis armature reaction at high temperature, the more the current increases, the larger the force difference is produced. The calculated force constants of the FOC and MFC were evaluated as 5.8 and 6.1 N/A, and the measured ones were as 5.9 and 6.2 N/A, respectively, in the given current range.

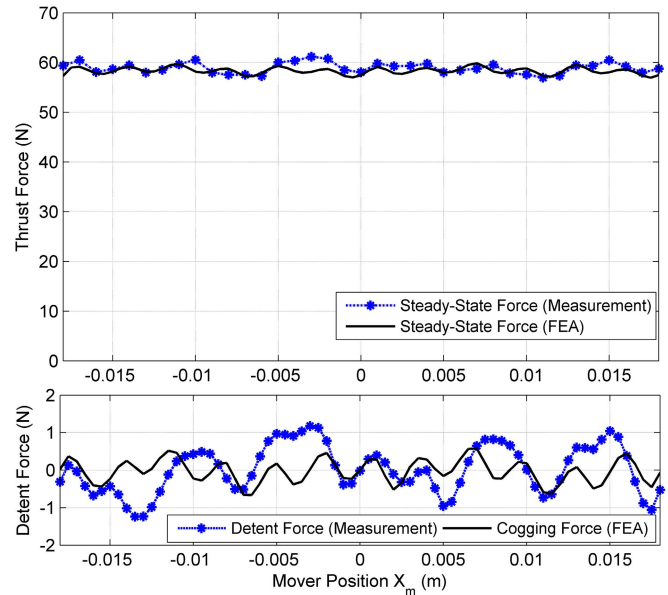


Fig. 19. Steady-state (top) force and detent (bottom) forces according to the mover positions when  $I_{qs}$  and  $I_{ds}$  are controlled as 10 and 0 A, respectively.

The measured force constants for both cases are slightly higher than the calculated ones. It seems that the residual flux density of the actual PM is slightly higher than that used in the calculation and FEA. These force constants also imply that the assumption for the unsaturated MEC model in Section III-A is reasonable in the armature current range of less than 10 A. This is because the MMF of the armature current in the small-sized PM machine is much less than that of the PM.

The force pulsation, also called force ripple, is caused by the detent force and the switching power circuit. Unlike the conventional rotary motor, the detent force in an iron-cored PM linear motor has not only the cogging force but also the end-effect force [12], [22], [23]. Furthermore, since the end-effect force acting on the complicated end frame in the linear motor exhibits the highly nonlinear behavior, there is no analytic solution for the end-effect force until now. Therefore, in this paper, the cogging force for the infinitely long stator model was simulated using 3-D FEA for the ripple-force comparison.

Fig. 19(top) and (bottom) shows the steady-state thrust forces when  $I_q = 10$  A and  $I_d = 0$  A, and the detent forces when  $I_q = I_d = 0$  A, respectively. The measured detent force in Fig. 19(bottom) shows that the cogging force predicted in an ideal FEA model is distorted by the residual harmonic term of the end-effect force. As a result, the actual detent force becomes much larger than the cogging force of the ideal FEA model. Thus, the peak-to-peak cogging force in the FEA model was evaluated as around 1.2 N, but the actual detent force was measured as 2.4 N, corresponding to approximately 2% and 4% of the rated thrust force. In addition, the resultant detent force directly affects the steady-state ripple force as shown in Fig. 19(top). Hence, the standard deviations of the steady-state forces in the FEA and measurement were evaluated as 0.81 and 1.13 N, respectively. The averages of the steady-state forces in the FEA and measurement were calculated as

58.4 and 58.9 N, respectively. Similar to the previous result, the measured average force has a 1% higher value than the simulated one.

## VI. CONCLUSION

Analytic modeling techniques were developed to analyze the double-sided IPM-FLBM with slot-phase shift and alternate teeth windings. A superposed winding function was established in the slot-phase shift configuration. The no-load flux linkages and back EMFs per phase were evaluated using this superposed winding technique, and its validity was verified by 3-D FEA. A variable winding function method was newly developed in order to evaluate the inductances of the linear motor configured with the salient iron core and alternate teeth winding. This technique improved the utility of the winding function in a specific structure. This was also sufficiently generalized to handle the same type of motor as an effective and reliable method. The steady-state thrust force model was derived using the parameters obtained from these models. In the end, the proposed models were verified and analyzed through the static force measurements in the MFC and FOC.

## REFERENCES

- [1] J. F. Gieras, Z. J. Piech, and B. Z. Tomczuk, "Topologies and selection," in *Linear Synchronous Motors*, 2nd ed. Boca Raton, FL, USA: CRC Press, 2012, pp. 1–22.
- [2] P. C. Sen, "Synchronous machines," in *Principles of Electric Machines and Power Electronics*, 2nd ed. Wiley, 1997, pp. 350–357.
- [3] H. Polinder, J. G. Sloopweg, M. J. Hoeijmakers, and J. C. Compter, "Modeling of a linear PM machine including magnetic saturation and end effects: Maximum force-to-current ratio," *IEEE Trans. Ind. Appl.*, vol. 39, no. 6, pp. 1681–1688, Nov./Dec. 2003.
- [4] B. Sheikh-Ghalavand, S. Vaez-Zadeh, and A. H. Isfahani, "An improved magnetic equivalent circuit model for iron-core linear permanent-magnet synchronous motors," *IEEE Trans. Magn.*, vol. 46, no. 1, pp. 112–120, Jan. 2010.
- [5] D. C. J. Krop, E. A. Lomonova, and A. J. A. Vandenput, "Application of Schwarz–Christoffel mapping to permanent-magnet linear motor analysis," *IEEE Trans. Magn.*, vol. 44, no. 3, pp. 352–359, Mar. 2008.
- [6] N. Bianchi, S. Bolognani, and F. Tonel, "Design criteria of a tubular linear IPM motor," in *Proc. Int. Conf. Electr. Mach. Drives*, vol. 1, Jun. 2001, pp. 1–7.
- [7] J. Wang, D. Howe, and G. W. Jewell, "Analysis and design optimization of an improved axially magnetized tubular permanent-magnet machine," *IEEE Trans. Energy Convers.*, vol. 19, no. 2, pp. 289–295, Jun. 2004.
- [8] K. J. Meessen, J. J. H. Paulides, and E. A. Lomonova, "Modeling and experimental verification of a tubular actuator for 20-g acceleration in a pick-and-place application," *IEEE Trans. Ind. Appl.*, vol. 46, no. 5, pp. 1891–1898, Sep./Oct. 2010.
- [9] M. Sanada, S. Morimoto, and Y. Takeda, "Interior permanent magnet linear synchronous motor for high-performance drives," *IEEE Trans. Ind. Appl.*, vol. 33, no. 4, pp. 966–972, Jul./Aug. 1997.
- [10] G. Stumberger, D. Zarko, M. T. Aydemir, and T. A. Lipo, "Design and comparison of linear synchronous motor and linear induction motor for electromagnetic aircraft launch system," in *Proc. IEEE Int. Conf. Electr. Mach. Drives*, vol. 1, Jun. 2003, pp. 494–500.
- [11] D. C. J. Krop, L. Encica, and E. A. Lomonova, "Analysis of a novel double sided flux switching linear motor topology," in *Proc. 19th Int. Conf. Electr. Mach.*, Sep. 2010, pp. 1–5.
- [12] Y.-S. Kwon and W.-J. Kim, "Detent-force minimization of double-sided interior permanent-magnet flat linear brushless motor," *IEEE Trans. Magn.*, vol. 52, no. 4, Apr. 2016, Art. no. 8201609.
- [13] D. Ishak, Z. Q. Zhu, and D. Howe, "Comparison of PM brushless motors, having either all teeth or alternate teeth wound," *IEEE Trans. Energy Convers.*, vol. 21, no. 1, pp. 95–100, Mar. 2006.
- [14] Z. Q. Zhu and D. Howe, "Instantaneous magnetic field distribution in brushless permanent magnet DC motors. III. Effect of stator slotting," *IEEE Trans. Magn.*, vol. 29, no. 1, pp. 143–151, Jan. 1993.
- [15] A. Balakrishnan, W. T. Joines, and T. G. Wilson, "Air-gap reluctance and inductance calculations for magnetic circuits using a Schwarz–Christoffel transformation," *IEEE Trans. Power Electron.*, vol. 12, no. 4, pp. 654–663, Jul. 1997.
- [16] J. Mühlethaler, J. W. Kolar, and A. Ecklebe, "A novel approach for 3D air gap reluctance calculations," in *Proc. 8th Int. Conf. Power Electron. ECCE Asia*, Jun. 2011, pp. 446–452.
- [17] J. Pyrhönen, T. Jokinen, and V. Hrabovcová, *Design of Rotating Electrical Machines*, 1st ed. New York, NY, USA: Wiley, 2008.
- [18] T. A. Lipo, *Analysis of Synchronous Machines*, 2nd ed. Boca Raton, FL, USA: CRC Press, 2012.
- [19] J. H. J. Potgieter and M. J. Kamper, "Evaluation of calculation methods and the effect of end-winding inductance on the performance of non overlap winding PM machines," in *Proc. 20th ICEM*, Mar. 2012, pp. 243–249.
- [20] N. A. Al-Nuaim and H. A. Toliyat, "A novel method for modeling dynamic air-gap eccentricity in synchronous machines based on modified winding function theory," *IEEE Trans. Energy Convers.*, vol. 13, no. 2, pp. 156–162, Jun. 1998.
- [21] D. W. Novotny and T. A. Lipo, *Vector Control and Dynamics of AC Drives*, 1st ed. London, U.K.: Oxford Univ. Press, 1996.
- [22] S. W. Youn, J. J. Lee, H. S. Yoon, and C. S. Koh, "A new cogging-free permanent-magnet linear motor," *IEEE Trans. Magn.*, vol. 44, no. 7, pp. 1785–1790, Jul. 2008.
- [23] Y.-W. Zhu, S.-G. Lee, K.-S. Chung, and Y.-H. Cho, "Investigation of auxiliary poles design criteria on reduction of end effect of detent force for PMLSM," *IEEE Trans. Magn.*, vol. 45, no. 6, pp. 2863–2866, Jun. 2009.

**Young-Shin Kwon** (S'11) received the B.S. degree in control and instrumentation engineering from Hanyang University, Seoul, South Korea, in 1995, and the M.S. degree in control and instrumentation engineering from Seoul National University, Seoul, in 1997. He is currently pursuing the Ph.D. degree with the Department of Mechanical Engineering, Texas A&M University, College Station, TX, USA.

He was the Automatic Transmission System Developer with Hyundai Electronics Corporation, Icheon, South Korea, for two years, after the M.S. degree. He also developed the active seekers of guided missile systems and naval/airborne radar systems as a Principal Researcher with LIG Nex1 Corporation, Yongin, South Korea, for thirteen years. His current research interests include design and analysis of spatial stabilization of multiaxis platforms, precision optomechanics systems, and linear magnetic actuators.

**Won-jong Kim** (S'89–M'97–SM'03) received the B.S. (*summa cum laude*) and M.S. degrees in control and instrumentation engineering from Seoul National University, Seoul, South Korea, in 1989 and 1991, respectively, and the Ph.D. degree in electrical engineering and computer science from the Massachusetts Institute of Technology, Cambridge, MA, USA, in 1997.

He has been with the Department of Mechanical Engineering, Texas A&M University, College Station, TX, USA, since 2000, where he is currently an Associate Professor. He was an Inaugural Holder of the Dietz Career Development Professorship II from 2007 to 2010. He holds three U.S. patents on precision positioning systems. His current research interests include the analysis, design, and real-time control of mechatronic systems, networked control systems, and nanoscale engineering and technology.

Prof. Kim is a fellow of ASME and a member of Pi Tau Sigma. He is or was the Technical Editor of the IEEE/ASME TRANSACTIONS ON MECHATRONICS, the *ASME Journal of Dynamic Systems, Measurement and Control*, the *International Journal of Control, Automation, and Systems*, and the *Asian Journal of Control*.